The effect of metal deposition order on the synergistic activity of Au–Cu and Au–Ce metal oxide catalysts for CO oxidation

S.A. Nikolaev [a,*], E.V. Golubina [a], I.N. Krotova [a], M.I. Shilina [a], A.V. Chistyakov [b], V.V. Kriventsov [c]

[a] Moscow State University, Leninskie Gory 1, Moscow 119991, Russia
[b] Topchiev Institute of Petrochemical Synthesis RAS, Leninskii pr. 29, Moscow 119991, Russia
[c] Boreskov Institute of Catalysis RAS, Pr. Akademika Lavrentieva 5, Novosibirsk 630090, Russia

ABSTRACT

Monometallic Au/Al_2O_3, M_xO_y/Al_2O_3 (M=Cu; Ce) catalysts and bimetallic catalysts with simultaneously $(Au + M_xO_y)$ and sequentially $(M_xO_y/Au, Au/M_xO_y)$ deposited metals were prepared. Oxidation of CO in the presence of these catalysts at 50–450 °C was studied. The activity of the catalysts increases in the following series: $M_xO_y/Au/Al_2O_3$ > $Au/M_xO_y/Al_2O_3$ > $(Au + M_xO_y)/Al_2O_3$ > Cu_xO_y/Al_2O_3 > Au/Al_2O_3 > Ce_xO_y/Al_2O_3. A synergistic effect was detected at 50–250 °C: bimetallic catalysts converted up to 50% of CO to CO_2, while the monometallic samples were inactive. Increasing the reaction temperature above 250 °C results in a decreased synergistic effect, although bimetallic catalysts still possess good activity. The electronic and structural organization of the catalyst active sites before and after the reaction were studied by means of XRD, TEM, EDX, XPS, and DRIFTS techniques. The causes for the synergistic effect and the reaction mechanism in the presence of synergistic catalysts are proposed and discussed.

© 2014 Elsevier B.V. All rights reserved.

1. Introduction

The first reference to gold as a catalyst dates back to 1906 when Bone and Wheeler observed oxidation of hydrogen on a heated gold gauze [1]. A number of papers dealing with catalytic hydrogenation of alkenes on gold films and impregnated gold catalysts were reviewed by Yolles et al. [2] and Bond and Sermon [3] in 70s. However, the original breakthrough in the catalysis by gold should be linked with Haruta et al., who demonstrated in 90s that gold can be an excellent catalyst when supported on metal oxides in a dispersed state [4]. The recent progress in heterogeneous catalysis resulted in remarkable investigations that showed the high activity of gold nanoparticles in the conversion of alcohols to synthetic hydrocarbons [5,6], selective oxidation of propene [7,8], synthesis of hydrogen peroxide [9,10], water gas shift reaction [11,12], hydrogenation of alkenes [13,14], isomerization [15,16], and hydrodechlorination [17,18].

The low-temperature CO oxidation catalyzed by gold nanoparticles has received most attention in both experimental [19–25] and theoretical [26–30] works. Supported Au–Cu and Au–Ce

compositions were found to be promising catalysts for low-temperature oxidation of CO due to their synergistic activity [31–36]. For example, Liu et al. reported that SBA-15-supported gold–copper, gold, and copper nanoparticles oxidize 79%, 36%, and 0% of CO at 25 °C, respectively [35]. Centeno et al. reported that Al_2O_3-supported gold–ceria, gold, and ceria nanoparticles oxidize 89%, 2%, and 0% of CO at 34 °C, respectively [36]. Although it is generally accepted that the high catalytic activity of monometallic gold catalysts can be attributed to the presence of small gold crystallites (<4 nm) [4,19], the nature of the most active sites in synergistic catalysts remains under discussion. Some authors consider that ionic gold provides the high activity observed for synergistic catalysts [37,38], others claim metallic gold to be the active sites [39], and third group of authors believes that the rough shape of particles [20], high oxygen capacity in bimetallic catalysts [40], the interface between gold and the second metal [19], the surface chemistry of bimetallic alloys [35] are of the first importance for synergistic activity.

This communication reports a comparative study of CO oxidation in the presence of synergistic Au–Cu and Au–Ce catalysts prepared by simultaneous and sequential deposition of the metals. To the best of our knowledge, this is the first study dealing with the effect of the metal deposition order in Au–Cu and Au–Ce catalysts on their synergistic activity. In order to reveal the nature of active sites in synergistic catalysts, the electronic and

* Corresponding author at: Faculty of Chemistry, Moscow State University, Leninskie Gory 1, Moscow 119991, Russia. Tel.: +7 495 9393498; fax: +7 495 9328846.
E-mail address: serge2000@rambler.ru (S.A. Nikolaev).

Table 1
Nominal and actual metal contents in the mono- and bimetallic catalysts.

Catalyst	Synthesis	Nominal metal content			Actual metal content		
		[Au]	[Cu]	[Ce]	[Au]	[Cu]	[Ce]
		wt.%	wt.%	wt.%	wt.%	wt.%	wt.%
Cu_xO_y/Al_2O_3	IMP	0	0.32	0	0	0.29	0
Ce_xO_y/Al_2O_3	IMP	0	0	0.71	0	0	0.68
Au/Al_2O_3 (IMP)	IMP	1.0	0	0	0.91	0	0
Au/Al_2O_3 (DP)	DP	1.0	0	0	0.76	0	0
$(Au + Cu_xO_y)/Al_2O_3$	IMP	1.0	0.32	0	0.72	0.32	0
$(Au + Ce_xO_y)/Al_2O_3$	IMP	1.0	0	0.71	0.78	0	0.57
$Au/Cu_xO_y/Al_2O_3$	DP/IMP	1.0	0.32	0	0.67	0.29	0
$Au/Ce_xO_y/Al_2O_3$	DP/IMP	1.0	0	0.71	0.73	0	0.61
$Cu_xO_y/Au/Al_2O_3$	IMP/DP	1.0	0.32	0	0.71	0.3	0
$Ce_xO_y/Au/Al_2O_3$	IMP/DP	1.0	0	0.71	0.68	0	0.55

morphological organizations of supported metal nanoparticles in the bimetallic catalysts and in their monometallic analogues were studied by means of X-ray diffraction (XRD), energy dispersive X-ray (EDX) analysis, transmission electron microscopy (TEM), X-ray photoelectron spectroscopy (XPS), and diffuse reflectance infrared Fourier transform spectroscopy (DRIFTS). The evolution of the catalyst surface during the reaction was also studied. Causes for the enhanced activity observed for bimetallic catalysts and characteristic features of the synergistic mechanism were proposed and discussed.

2. Experimental

2.1. Catalyst preparation

Gamma alumina (Catalyst LLC, $S = 160\,m^2/g$) was used as a support for catalysts; $Cu(NO_3)_2$, $Ce(NO_3)_3$, and $HAuCl_4$ (Sigma–Aldrich, 98–99% pure) were used as metal precursors. Cu_xO_y/Al_2O_3, Ce_xO_y/Al_2O_3 and Au/Al_2O_3 (IMP) catalysts were prepared by impregnation (IMP). In IMP synthesis, the calculated amount of metal precursor containing 2.5×10^{-4} mol of the metal was dissolved in 5.5 ml of H_2O. The support (5.0 g) was added to the solution, dried at 25 °C for 24 h and calcined at 400 °C in air for 3 h. Au/Al_2O_3 (DP) catalyst was prepared by deposition-precipitation (DP). In DP synthesis, the calculated amount of $HAuCl_4$ containing 2.5×10^{-4} mol of Au was dissolved in 40 ml of H_2O. The pH of the solution was adjusted to 7.0 by addition of 0.1 M NaOH. The support (5.0 g) was dispersed in the solution with stirring at 50 °C for 1 h. The solid was washed with water (4 l), dried at 25 °C for 24 h and calcined at 400 °C in air for 3 h.

The bimetallic $(Au + Cu_xO_y)/Al_2O_3$ catalyst was produced by simultaneous deposition of metals. The calculated amounts of $HAuCl_4$ (2.5×10^{-4} mol of Au) and $Cu(NO_3)_2$ (2.5×10^{-4} mol of Cu) were dissolved in 5.5 ml of H_2O. Alumina (5.0 g) was added to the solution, dried at 25 °C for 24 h and calcined at 400 °C in air for 3 h. The $(Au + Ce_xO_y)/Al_2O_3$ catalyst was produced by the technique used to manufacture the $(Au + Cu_xO_y)/Al_2O_3$ catalyst. The $Au/Cu_xO_y/Al_2O_3$ catalyst was produced by deposition of gold on the Cu_xO_y/Al_2O_3 catalyst. The calculated amount of $HAuCl_4$ (1.25×10^{-4} mol of Au) was dissolved in 20 ml of H_2O. The pH of the solution was adjusted to 7.0 by addition of 0.1 M NaOH. The Cu_xO_y/Al_2O_3 catalyst (2.5 g) was dispersed in the solution with stirring at 50 °C for 1 h. The sample obtained was washed with water, dried at 25 °C for 24 h and calcined at 400 °C in air for 3 h. The $Au/Ce_xO_y/Al_2O_3$ catalyst was produced deposition of gold on the Ce_xO_y/Al_2O_3 by the technique used to manufacture $Au/Cu_xO_y/Al_2O_3$. The $Cu_xO_y/Au/Al_2O_3$ catalyst was produced by deposition of Cu_xO_y on the Au/Al_2O_3 catalyst. The calculated amount of $Cu(NO_3)_2$ (1.25×10^{-4} mol of Cu) was dissolved in 2.75 ml of H_2O. The Au/Al_2O_3 (DP) catalyst (2.5 g) was added to

2.75 ml of the solution dried at 25 °C for 24 h and calcined at 400 °C in air for 3 h. The $Ce_xO_y/Au/Al_2O_3$ catalyst was produced by deposition of Ce_xO_y on the Au/Al_2O_3 (DP) by the technique used to manufacture the $Cu_xO_y/Au/Al_2O_3$ catalyst.

The desired Cu, Ce, and Au contents in the catalysts were 0.32, 0.71, and 1 wt.%, respectively. These contents correspond to equimolar Au/M ratio. The actual metal content was determined by atomic absorption spectroscopy (AAS) on a Thermo iCE 3000 AA spectrometer. A catalyst (0.1 g) was treated with 10 ml of aqua regia (HCl: HNO_3 = 4:1) for 1 h. This mixture was added to 90 ml of H_2O. The metal contents in the solution were measured by AAS with application of the calibration curves. The actual metal content in the catalyst $[C_1]$ was calculated as $[C_1] = [C_2] \times V \times m^{-1} \times 100\%$, where $[C_2]$ is the metal content in the solution measured by AAS, $[V]$ is the volume of the analyzed solution, and $[m]$ is the mass of the analyzed catalyst. The details of mono- and bimetallic catalysts are listed in Table 1.

2.2. Catalyst characterization

TEM measurements were carried out on a JEOL JEM 2100 F/UHR microscope with 0.1-nm resolution. Analyzed specimens were prepared by ultrasonic dispersion of the catalysts (0.2 g) in ethanol (10 ml) followed by deposition of a drop of suspension on a carbon-coated grid. The assignment of dark spots visible in the TEM images to the metal particles and determination of the quantitative composition of particles was performed by means of EDX analysis with application of a JED-2300 X-ray spectrometer. The HRTEM images of the mono- and bimetallic catalysts and EDX spectra are presented in Supplementary material (Figs. S1–S12). The size of particles was calculated as maximum linear size. For each catalyst, 300–380 particles were processed to determine the particles size distribution. The small particles with the size of 1–4 nm were determined as SML particles. The spherical and nonspherical shape of the particles was determined as SPH and NSPH, respectively.

XRD analysis of the catalysts was carried out on a Rigaku D/MAX 2500 instrument using $CuK\alpha$ radiation with a step size of 0.02° two-theta (2θ) ranging from 35 to 70°. XPS analysis of the catalysts was performed on a Kratos Axis Ultra DLD spectrometer using $AlK\alpha$ radiation (1486.6 eV). The binding energies were corrected by referencing to the internal standard -Al 2p (74.6 eV).

DRIFT spectra of adsorbed CO were recorded using an InfraLUM FT-801 spectrometer with $4\,cm^{-1}$ resolution ranging from 900 to $6000\,cm^{-1}$. Accumulation of 128 scans was used for collecting each spectrum. In a typical experiment, 0.04 g of catalyst was loaded to the DRIFT cell and heated in vacuum at 400 °C for 2 h. The cell was cooled to 25 °C and then a background spectrum (A) was recorded. The equilibrium CO pressure (0.4–1.5 kPa) was added to the sample at 25 °C and then a spectrum (B) was recorded. The final
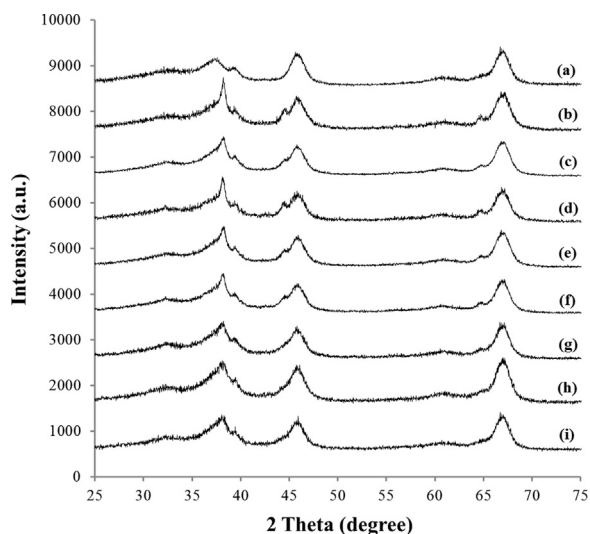
Fig. 1. XRD patterns of the support and catalysts. (a) Al_2O_3: the XRD pattern of Cu_xO_y/Al_2O_3 and Ce_xO_y/Al_2O_3 is similar to the XRD pattern of Al_2O_3; (b) Au/Al_2O_3 (IMP); (c) Au/Al_2O_3 (DP); (d) $(Au + Cu_xO_y)/Al_2O_3$; (e) $(Au + Ce_xO_y)/Al_2O_3$; (f) $Au/Cu_xO_y/Al_2O_3$; (g) $Au/Ce_xO_y/Al_2O_3$; (h) $Cu_xO_y/Au/Al_2O_3$; (i) $Ce_xO_y/Au/Al_2O_3$.

spectrum was obtained by subtracting spectrum A from spectrum B and transformed into Kubelka–Munk units.

2.3. CO oxidation

The reaction was carried out under atmospheric pressure in a quartz reactor at 50–450 °C with a step size of 50 °C. A helium at a total flow rate of 70 ml/min (gas hourly space velocity: 46,700 h^{-1}) was passed through the reactor during the experiments. A gas mixture (2 vol.% CO + 1 vol.% O_2 + 97 vol.% He) was introduced as the reactants. In a typical experiment, 0.1 g (i.e., 0.09 ml) of a catalyst was loaded into the reactor, cleaned with helium at 450 °C for 1 h, and cooled to the desired temperature. A pulse of reactants (1 ml) was added to the reactor. The quantitative composition of the flow at the reactor inlet and outlet was determined by GC on an LHM-80 gas chromatograph equipped with a thermal conductivity detector and a packed column (Porapak Q, 1 m, id 2 mm). Carbon monoxide conversion was calculated from CO and CO_2 peak areas using pre-constructed calibration curves. Ten to thirty reactant pulses were introduced in order to obtain steady-state CO conversion value at each temperature.

3. Results and discussion

3.1. Phase composition, dispersion, and crystallinity of the catalysts

Six diffraction peaks at 2θ of 32.5°, 37.6°, 39.5°, 46.0°, 61.1°, and 66.8° were observed for the support (Fig. 1(a)), which were assignable to (1 1 1), (2 2 0), (3 1 1), (2 2 2), (4 0 0), (5 1 1), and (4 4 0) reflections of γ-Al_2O_3 [41]. The XRD patterns of Cu_xO_y/Al_2O_3 and Ce_xO_y/Al_2O_3 catalysts are indistinguishable from the XRD pattern recorded for the support. This result could be explained by the high dispersion of Cu_xO_y and Ce_xO_y particles [6], their amorphous state [31] or relatively low concentration of supported metals. Three new diffraction peaks at 2θ of 38.1°, 44.4°, and 64.6° were observed for the Au/Al_2O_3 (IMP) and Au/Al_2O_3 (DP) catalysts (Fig. 1(b) and (c)). New peaks were attributed to (1 1 1), (2 0 0), and (2 2 0) reflections of cubic gold [11,36]. The diffraction peaks of gold observed for the Au/Al_2O_3 (DP) catalyst were broader in comparison with those observed for the Au/Al_2O_3 (IMP) catalyst, suggesting a smaller gold
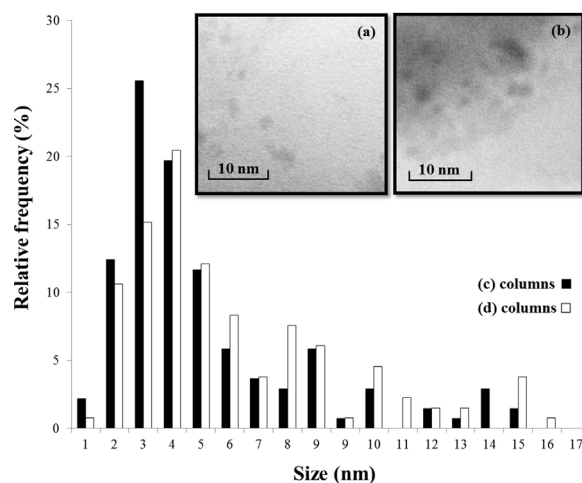
particle size in the Au/Al_2O_3 (DP). This result is in agreement with the reported data [15,34].

The XRD patterns of Au–Cu and Au–Ce catalysts possess the diffraction peaks of alumina and gold. No Cu or Ce peaks were observed for bimetallic catalysts (Fig. 1(d)–(h)). Liu et al. [35] observed the shift of diffraction peaks of gold toward high angles for Au–Cu/SBA-15 catalyst. This shift was attributed to the formation of Au–Cu alloy. The shifts of gold peaks for our bimetallic catalysts were not observed, thus the formation of Au–M alloys in our catalysts is not supported. The diffraction peaks of gold observed for the Au–Cu and Au–Ce catalysts were broader in comparison with the gold peaks observed for the Au/Al_2O_3 catalysts (Fig. 1(b)–(h)), suggesting a smaller Au particle size in bimetallic samples. This result can be explained by anchoring of small gold particles near the supported copper or cerium particles [19–23,35].

3.2. Size and shape of the supported metal nanoparticles

The TEM images of catalysts and the particles size distributions are presented in Figs. 2–6, S1 and S2. The results of morphological analysis of the catalysts are summarized in Table 2. The shape of Cu_xO_y and Ce_xO_y particles before oxidation in the Cu_xO_y/Al_2O_3 and Ce_xO_y/Al_2O_3 catalysts was nearly spherical (SPH)—Fig. 2(a) and (b). A narrow particle size distribution with the mean size of
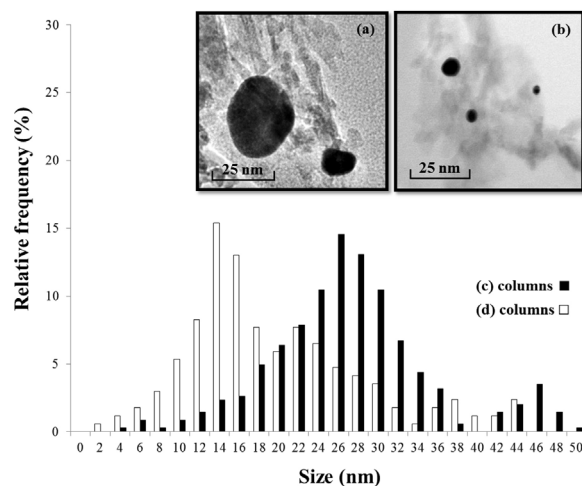

Fig. 2. Size and shape of supported particles in (a) Cu_xO_y/Al_2O_3 and (b) Ce_xO_y/Al_2O_3. Particle size distribution for (c) Cu_xO_y/Al_2O_3 and (d) Ce_xO_y/Al_2O_3.

Fig. 3. Size and shape of supported particles in (a) Au/Al_2O_3 (IMP) and (b) Au/Al_2O_3 (DP). Particle size distribution for (c) Au/Al_2O_3 (IMP) and (d) Au/Al_2O_3 (DP).

Table 2
Structural organization of supported metal particles for the catalysts. D is the mean particle size, [SML] is the relative content of 1–4 nm particles, [SPH] is the relative content of spherical particles, [NSPH] is the relative content of nonspherical particles.

Catalyst	Before CO oxidation				After CO oxidation at 450 °C			
	D	[SML]	[SPH]	[NSPH]	D	[SML]	[SPH]	[NSPH]
	nm	%	%	%	nm	%	%	%
Cu_xO_y/Al_2O_3	3	60	99.7	0.3	3.5	56	99.9	0.1
Ce_xO_y/Al_2O_3	4	47	99.9	0.1	4	40	99.8	0.2
Au/Al_2O_3 (IMP)	27	0.3	99.5	0.1	36	0.1	99.8	0.2
Au/Al_2O_3 (DP)	15	1.8	98.3	0.2	19	1.3	98.7	0.3
$(Au+Cu_xO_y)/Al_2O_3$	20	2.9	98.8	1.2	25	1.6	99.3	0.7
$(Au+Ce_xO_y)/Al_2O_3$	18	4.1	96.2	3.8	22	2.2	96.6	3.4
$Au/Cu_xO_y/Al_2O_3$	9	8.7	93.6	6.4	10	5.9	94.9	5.1
$Au/Ce_xO_y/Al_2O_3$	10	5.1	94	6.0	11	4.2	95.1	4.9
$Cu_xO_y/Au/Al_2O_3$	6	25	73	27	7	21	76	24
$Ce_xO_y/Au/Al_2O_3$	8	14	81	19	8	10	87	13

3–4 nm was observed for these catalysts (Fig. 2(c) and (d)). The relative content of small (SML) particles with the size of 1–4 nm in the Cu_xO_y/Al_2O_3 and Ce_xO_y/Al_2O_3 catalysts was high (47–60%). The small size of Cu_xO_y and Ce_xO_y particles revealed by TEM is in good agreement with the results of XRD analysis discussed in Section 3.1. The SPH shape of supported particles and the high

concentration of SML particles were retained after the reaction in the Cu_xO_y/Al_2O_3 and Ce_xO_y/Al_2O_3 catalysts (Table 2). The mean size of particles increased by 0.2–0.5 nm after oxidation at 450 °C (Table 2), indicating high resistance of Cu_xO_y and Ce_xO_y particles to sintering, which can be explained by strong metal-support interaction [19].

The shape of Au particles before oxidation in the Au/Al_2O_3 (IMP) and (DP) catalysts was SPH (Fig. 3(a) and (b)); Figs. S1, S3 and S4. A broad particle size distribution was observed for these catalysts (Fig. 3(c) and (d)). The mean size of gold particles in the Au/Al_2O_3 (IMP) catalyst was 27 nm, which is twice as high as that in the Au/Al_2O_3 (DP) catalyst (Table 2). This result, together with the low content of SML particles observed in the Au/Al_2O_3 (IMP) catalyst is indicative of a weaker metal-support interaction in the IMP catalyst compared to the DP catalyst. The SPH shape of particles in the monometallic gold catalysts was retained after the reaction at 450 °C (Table 2). Heating of the Au/Al_2O_3 catalysts during the reaction resulted in increase in the mean gold particles size by 4–9 nm accompanied by a decrease in the content of SML particles (Table 2), which is in line with the low resistance of gold clusters to sintering reported previously [19].

The TEM image of the $(Au+Cu_xO_y)/Al_2O_3$ catalyst produced by simultaneous metal deposition before oxidation is presented in Fig. 4(a). A broad particles size distribution with the mean size of 20 nm was observed for this catalyst (Fig. 4(c)). The morphological features concerning the mean particle size and the SML content in the $(Au+Cu_xO_y)/Al_2O_3$ catalyst indicate that the presence of copper species prevents the IMP gold clusters from sintering (Table 2,
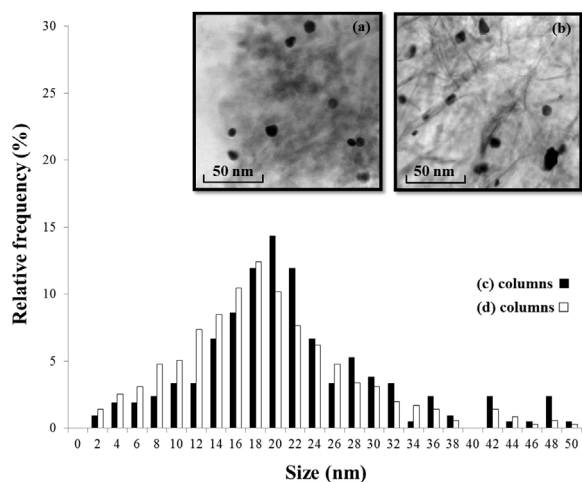

Fig. 4. Size and shape of particles in (a) $(Au+Cu_xO_y)/Al_2O_3$ and (b) $(Au+Ce_xO_y)/Al_2O_3$. Particle size distribution for (c) $(Au+Cu_xO_y)/Al_2O_3$ and (d) $(Au+Ce_xO_y)/Al_2O_3$.

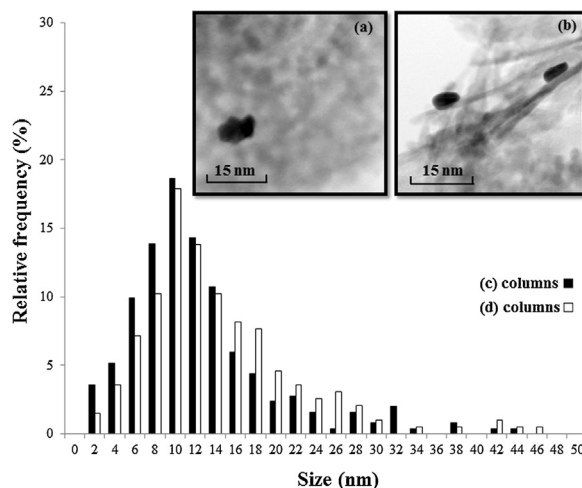**Fig. 5.** Size and shape of particles in (a) $Au/Cu_xO_y/Al_2O_3$ and (b) $Au/Ce_xO_y/Al_2O_3$. Particle size distribution for (c) $Au/Cu_xO_y/Al_2O_3$ and (d) $Au/Ce_xO_y/Al_2O_3$.
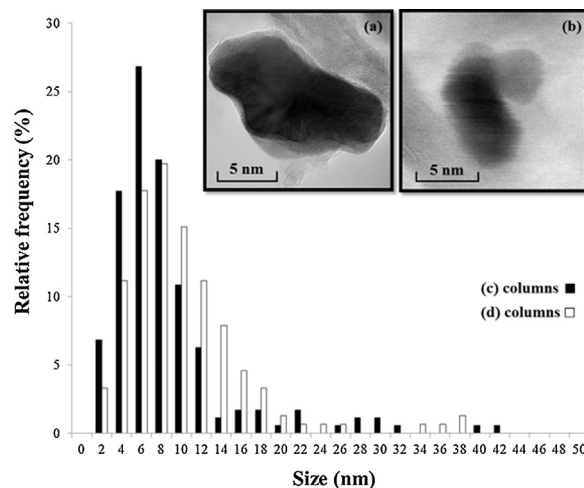

Fig. 6. Size and shape of particles in (a) $Cu_xO_y/Au/Al_2O_3$ and (b) $Au/Ce_xO_y/Al_2O_3$. Particle size distribution for (c) $Cu_xO_y/Au/Al_2O_3$ and (d) $Ce_xO_y/Au/Al_2O_3$.

cf. $(Au + Cu_xO_y)/Al_2O_3$ and its monometallic precursor Au/Al_2O_3 (IMP)), which agrees with the reported data [35]. This is also in agreement with the results of XRD analysis discussed in Section 3.1. According to TEM-EDX analysis, the $(Au + Cu_xO_y)/Al_2O_3$ catalyst contains 98.8% of SPH and 1.2% of non-spherical (NSPH) gold particles with the size of 4–10 nm. Note that some large agglomerates of gold clusters with the size of 34–60 nm were also detected in the Au/Al_2O_3 catalysts (Fig. S2), but their content was significantly lower (0.1–0.3%). According to TEM-EDX analysis, most of the NSPH particles detected in the $(Au + Cu_xO_y)/Al_2O_3$ catalyst were situated near copper species. Thus, the presence of small NSPH gold particles in the $(Au + Cu_xO_y)/Al_2O_3$ catalyst may be caused by distortion of SPH gold clusters situated near Cu_xO_y species upon sintering of gold during catalyst calcination.

The TEM image of the $(Au + Ce_xO_y)/Al_2O_3$ catalyst produced by simultaneous metal deposition before oxidation is presented in Fig. 4(b). The mean particle size in this catalyst was 18 nm (Fig. 4(d)) and the content of SML particles was 4.1% (Table 2), indicating that gold clusters are prevented from sintering in the presence of Ce_xO_y (Table 2), cf. $(Au + Ce_xO_y)/Al_2O_3$ and its monometallic precursor Au/Al_2O_3 (IMP)). The morphological features concerning the mean particle size and the SML content indicate that gold clusters are better dispersed in the $(Au + Ce_xO_y)/Al_2O_3$ catalyst than in the $(Au + Cu_xO_y)/Al_2O_3$ catalyst (Table 2). The content of small NSPH gold particles was also higher in the $(Au + Ce_xO_y)/Al_2O_3$ catalyst than in the $(Au + Cu_xO_y)/Al_2O_3$ catalyst. Heating the $(Au + M_xO_y)/Al_2O_3$ catalysts produced by simultaneous metal deposition during the CO oxidation resulted in increase in the mean particle size by 4–5 nm, decrease in SML particle concentration by 1.3–1.9% and decrease in NSPH particle concentration by 0.4–0.5% (Table 2).

The initial bimetallic $Au/M_xO_y/Al_2O_3$ and $M_xO_y/Au/Al_2O_3$ catalysts produced by sequential metal deposition were found to contain both SPH and NSPH gold particles. This result, together with the data discussed above suggest similar qualitative structural organizations for the supported particles in catalysts produced by sequential metal deposition and in catalysts produced by simultaneous metal deposition (Figs. 4–6(a)–(d)). An important feature of catalysts produced by sequential metal deposition compared with catalysts produced by simultaneous metal deposition is better surface stabilization of small gold clusters (Table 2). This is confirmed by the high content of SML particles (up to 25%) and small mean particle size (up to 6 nm). The resistance of SML gold clusters to sintering was also higher in the bimetallic $Au/M_xO_y/Al_2O_3$ and $M_xO_y/Au/Al_2O_3$ catalysts than in the bimetallic $(Au + M_xO_y)/Al_2O_3$ catalysts. The final important characteristic of the $Au/M_xO_y/Al_2O_3$ and $M_xO_y/Au/Al_2O_3$ catalysts is the relatively high content of NSPH gold particles (up to 27%), which is preserved upon heating up to 450 °C during the CO oxidation (Table 2).

3.3. Oxidation states of the supported metal nanoparticles

In order to analyze the oxidation states of the supported metal species in the catalysts, two independent techniques (XPS and DRIFTS) were applied and the results are presented in Figs. 7–11. The Cu 2p spectrum of the Cu_xO_y/Al_2O_3 catalyst before oxidation is shown in Fig. 7(a). It exhibits a doublet of two spin orbit components: Cu $2p_{3/2}$ (932.5 eV) and Cu $2p1/2$ (952.6 eV). These binding energies can be attributed to Cu_2O and/or Cu^0 species [37,42]. A peak at 944 eV was observed for the Cu_xO_y/Al_2O_3 catalyst. This satellite is the unique feature of CuO spectrum and is absent in XPS spectra of Cu_2O and/or Cu^0 species [43]. The precise quantification of Cu^0, Cu^+, and Cu^{2+} contents is a rather difficult task due to overlapping of XPS signals from Cu^0, Cu^+, and Cu^{2+} electrons in the Cu $2p_{3/2}$ and Cu $2p_{1/2}$ regions. Nevertheless, the $([Cu^0] + [Cu^+])/[Cu^{2+}]$ ratio can be roughly estimated. Biesinger et al. reported that the
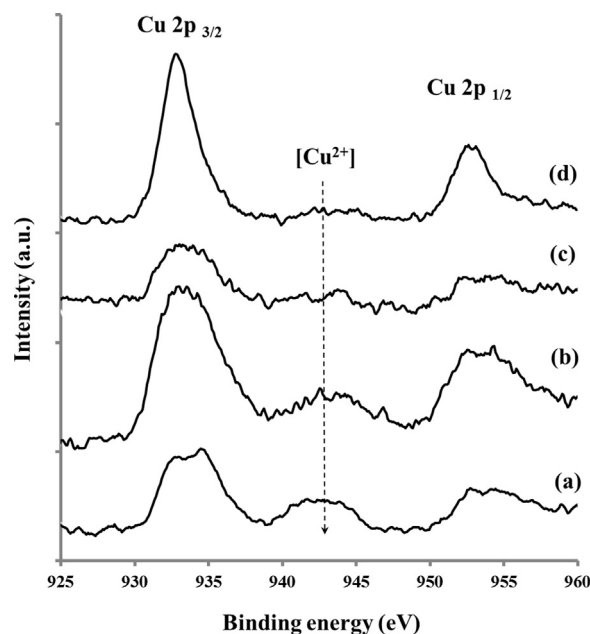
Fig. 7. Cu 2p XPS spectra for mono- and bimetallic catalysts. (a) Cu_xO_y/Al_2O_3; (b) $(Au + Cu_xO_y)/Al_2O_3$; (c) $Au/Cu_xO_y/Al_2O_3$; (d) $Cu_xO_y/Au/Al_2O_3$.

area of Cu^{2+} satellite is twice lower than the area of Cu $2p_{3/2}$ peak for the Cu^{2+} species [43]. Bearing this in mind, the $([Cu^0] + [Cu^+])/[Cu^{2+}]$ ratio for the Cu_xO_y/Al_2O_3 catalyst should be about 1/7.

The DRIFT spectra of CO surface species for Al_2O_3 and Cu_xO_y/Al_2O_3 catalyst before the reaction are shown in Fig. 8(a) and (b). The adsorption of CO on Al_2O_3 produced a single band at about 2203 cm^{-1}, which is assignable to the Al^{+3}–CO carbonyl [44]. The adsorption of CO on the Cu_xO_y/Al_2O_3 catalyst produced new bands at about 2103 and 2142 cm^{-1}, which are assignable to Cu^0–CO and Cu^+–CO carbonyls [42,45,46]. No bands for surface Cu^{2+} carbonyls were detected, which may be due to weak and reversible adsorption of CO on Cu^{2+} species at 25 °C [44,47]. The detection of the Cu^0–CO carbonyl may be caused by the presence of Cu^0 in the initial Cu_xO_y/Al_2O_3 catalyst (this is less probable, because the catalyst was not reduced before use) or by reduction of the cationic copper by CO (this is more probable and is in agreement with the reported
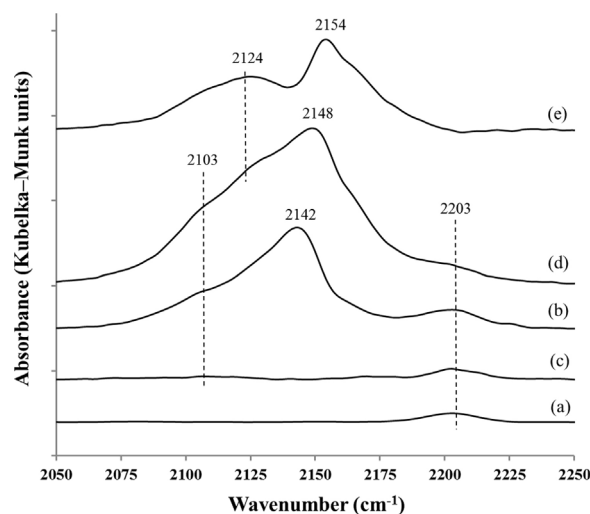
Fig. 8. DRIFT spectra of CO adsorption on Al_2O_3, Au, Cu, and Au–Cu catalysts. (a) Al_2O_3; (b) Cu_xO_y/Al_2O_3; (c) Au/Al_2O_3 (DP); (d) $Cu_xO_y/Au/Al_2O_3$; (e) difference spectrum ((d)–(b)–(c)). The spectra were recorded at 25 °C under constant CO pressure (0.4 kPa).

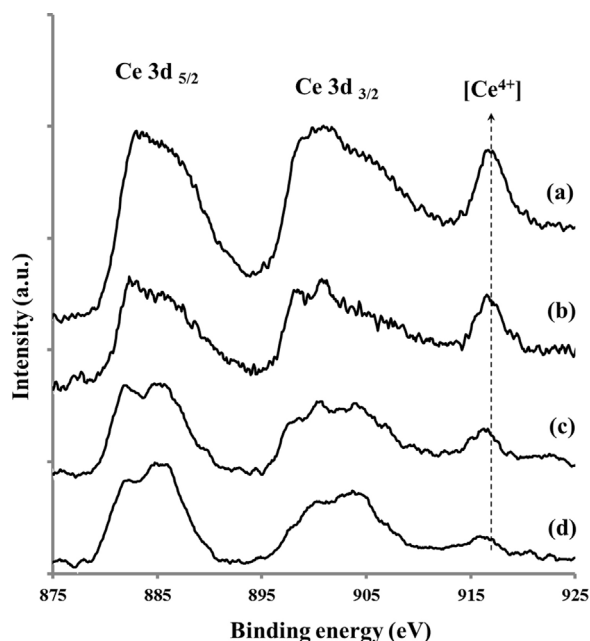**Fig. 9.** Ce 3d XPS spectra for mono- and bimetallic catalysts. (a) Ce_xO_y/Al_2O_3; (b) $(Au + Ce_xO_y)/Al_2O_3$; (c) $Au/Ce_xO_y/Al_2O_3$; (d) $Ce_xO_y/Au/Al_2O_3$.

data [44]). In fact, the most important information is that the band at about $2103\ cm^{-1}$ was significantly less intense than the band at about $2142\ cm^{-1}$, indicating that the Cu^0 content is negligible compared to the Cu^+ content in the Cu_xO_y/Al_2O_3 catalyst.

The Ce 3d spectrum of the Ce_xO_y/Al_2O_3 catalyst before oxidation is presented in Fig. 9(a). The peaks at about 875–895 eV correspond to the Ce $3d_{5/2}$ spin orbit components and the peaks at about 895–910 eV correspond to the Ce $3d_{3/2}$ spin orbit components. The peaks at 880.2, 885.0, 899.5, and 903.5 eV are indicative of Ce_2O_3 as opposed to those at 882.1, 888.1, 898.0, 900.9, 906.4, and 916.40 eV, which are due to the presence of CeO_2 as reported in [48–51]. A comparison of our spectrum with the XPS data reported in [48–50] demonstrates that cerium in the Ce_xO_y/Al_2O_3 catalyst exists as a mixture of Ce_2O_3 and CeO_2. A peak at 916.7 eV was observed for the Ce_xO_y/Al_2O_3 catalyst. This satellite is a part of the CeO_2 spectrum and is absent in the spectrum of Ce_2O_3 [49]. The surface chemistry

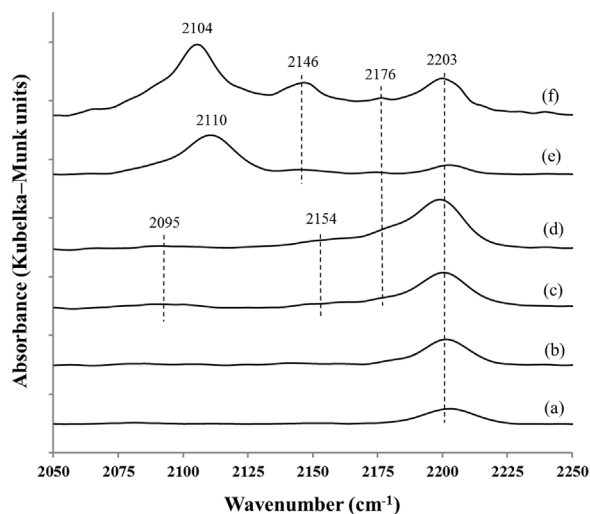**Fig. 10.** DRIFT spectra of CO adsorption on Ce and Au–Ce catalysts. The spectra for the Ce_xO_y/Al_2O_3 catalyst were recorded at 25 °C under a CO pressure of (a) 0.4 kPa; (b) 0.8 kPa; (c) 1.2 kPa; and (d) 1.5 kPa. The spectra for the $Ce_xO_y/Au/Al_2O_3$ catalyst were recorded at 25 °C under a CO pressure of (e) 0.4 kPa and (f) 1.5 kPa.
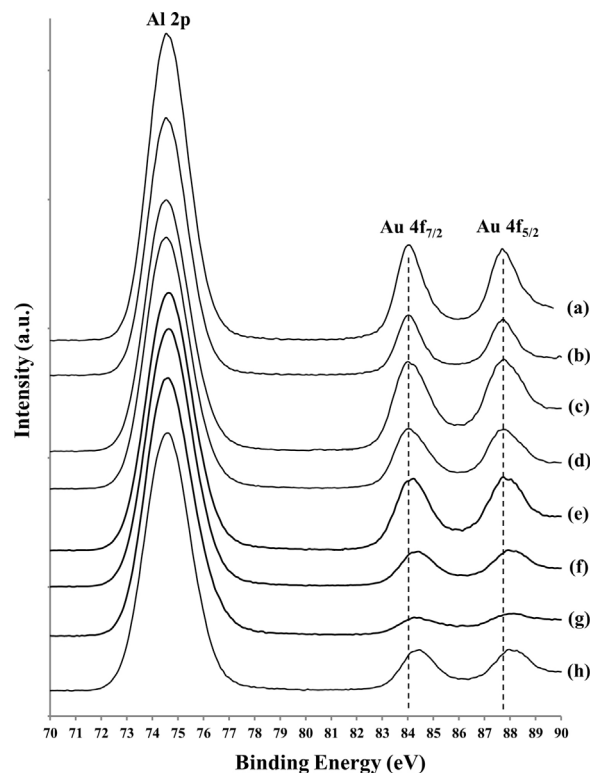

Fig. 11. Al 2p and Au 4f XPS spectra for mono- and bimetallic catalysts. (a) Au/Al_2O_3 (IMP); (b) Au/Al_2O_3 (DP); (c) $(Au + Cu_xO_y)/Al_2O_3$; (d) $(Au + Ce_xO_y)/Al_2O_3$; (e) $Au/Cu_xO_y/Al_2O_3$; (f) $Au/Ce_xO_y/Al_2O_3$; (g) $Cu_xO_y/Au/Al_2O_3$; (h) $Ce_xO_y/Au/Al_2O_3$. The vertical lines show the binding energies of Au^0.

of the Ce_xO_y/Al_2O_3 catalyst (2 wt.% Ce) was studied in [51] and it was mentioned that the area of the Ce^{4+} satellite is about 20% of the area of Ce 3d peaks. Considering these data, the $[Ce^{3+}]/[Ce^{4+}]$ ratio for the Ce_xO_y/Al_2O_3 catalyst should be about 1/2.

The DRIFT spectra for the Ce_xO_y/Al_2O_3 catalyst are presented in Fig. 10(a)–(d). Carbon monoxide does not interact with the ceria sites of the Ce_xO_y/Al_2O_3 catalyst at low CO pressure, since no bands were observed at 2120–$2140\ cm^{-1}$ (Ce^{3+}–CO) or 2170–$2190\ cm^{-1}$ (Ce^{4+}–CO) [52,53]. An increase in the CO pressure gave rise to bands at about 2154 and $2176\ cm^{-1}$, which were assigned to Ce^{3+} and Ce^{4+} carbonyls, and a weak band at about $2095\ cm^{-1}$, which may be due to the reduction of cationic cerium with CO. The qualitative composition of the catalyst surface determined by DRIFTS coincides with that elucidated from the XPS data.

The Au 4f spectra of gold-contained catalysts before oxidation are presented in Fig. 11(a)–(h). These spectra exhibit a doublet of two spin orbit components: Au $4f_{7/2}$ (at about 84 eV) and Au $4f_{5/2}$ (at about 88 eV). The oxidation state of gold is usually determined from the position of the Au $4f_{7/2}$ peak. It is generally accepted that the Au $4f_{7/2}$ binding energies of 83.9–84.0, 84.4–84.8, and 85.1–85.4 eV are assigned to Au^0, Au_2O, and Au_2O_3, respectively [19,37,40]. The intermediate values can be assigned to a mix of gold and its oxides [37,54]. The value of Au 4f 7/2 binding energies for the Au/Al_2O_3 (IMP) and Au/Al_2O_3 (DP) were 83.8–83.9, indicating the presence of Au^0 species (Fig. 11(a) and (b)), which is in agreement with our DRIFTS measurements: a band at about $2103\ cm^{-1}$ attests to the presence of the Au^0CO carbonyl (Fig. 8(c)). A slight positive shift of the Au $4f_{7/2}$ peak was observed for the bimetallic catalysts produced by simultaneous metal deposition, which indicates the formation of some $Au^{\delta+}$ species in catalysts. The positive shift of the Au $4f_{7/2}$ peak was accompanied by a decrease in the relative areas of Cu^{2+} and Ce^{4+} satellites, indicating that the Cu^+ and Ce^{3+} concentrations in the bimetallic catalysts increased (Fig. 11(c) and (d); Fig. 7(b);

Fig. 9(b). A more pronounced shift of Au $4f_{7/2}$ peak by 0.1–0.3 eV and a greater decrease in the relative areas of Cu^{2+} and Ce^{4+} satellites were observed for the bimetallic catalysts produced by sequential metal deposition (Fig. 11(e)–(h); Fig. 7(c) and (d); Fig. 9(c) and (d)).

The formation of $Au^{\delta+}$ accompanied by reduction of CuO and CeO_2, which was observed for our bimetallic catalysts, is in agreement with the reported data [38,55–57]. Duh et al. found that CuO is converted to Cu_2O after deposition of Au to the CuO/TiO_2 catalyst [38]. The positive shift of Au 4f peaks was also detected. Sugano et al. reported that the surface of Au–Cu/P25 consists of Cu_2O produced by reduction of CuO by plasmon-activated gold atoms [57]. Pestryakov et al. reported that the addition of Ce_xO_y and Zr_xO_y to Au clusters stabilizes the $Au^{\delta+}$ ($0 < \delta < 1$) oxidation state due to electron transfer from gold to the metal oxide [55]. The reduction of Ce^{4+} to Ce^{3+} after deposition of Au on CeO_2 (1 1 1) was observed by Škoda et al. [58].

In order to verify XPS results, the $M_xO_y/Au/Al_2O_3$ catalysts with the most pronounced electronic changes were chosen and DRIFTS measurements were conducted. The adsorption of CO on the $Cu_xO_y/Au/Al_2O_3$ catalyst produced a broad asymmetric band at about 2148 cm^{-1} Fig. 8(d). This band is shifted by 6 cm^{-1} to higher frequencies with respect to the band assigned to Cu^+–CO carbonyl in the Cu_xO_y/Al_2O_3 catalyst (Fig. 8(b) and (d)). Both the asymmetric shape of the band at about 2148 cm^{-1} and its positive shift indicate the formation of new adsorption sites. In order to clarify the nature of these sites, the subtracting procedure was conducted. The resulting spectrum ($Cu_xO_y/Au/Al_2O_3$–Cu_xO_y/Al_2O_3–Au/Al_2O_3 (DP)) shows bands at about 2124 and 2154 cm^{-1} (Fig. 8(e)). Davydov and Sheppard [44] and Bailie et al. [45] assigned the bands at about 2120 and 2136 cm^{-1} to $Cu^{\sigma+}$ – CO ($0 < \sigma < 1$) and Cu^+–CO carbonyls, respectively. Centeno et al. [36] and Klimev et al. [59] reported that bands in the 2130–2155 cm^{-1} range are assignable to $Au^{\delta+}$–CO ($0 < \delta < 1$). According to these data, we can assign the bands at about 2124 and 2154 cm^{-1} to carbonyls formed with the participation of $Cu^{\sigma+}$ ($0 < \sigma < 1$) and $Au^{\delta+}$ ($0 < \delta < 1$) sites, which is in agreement with the XPS results of the current work.

The adsorption of CO on the $Ce_xO_y/Au/Al_2O_3$ catalyst gave rise to bands at about 2110, 2146, and 2176 cm^{-1} even at low CO pressure (Fig. 10(e)). An increase in the CO pressure resulted in increase in the intensity of these bands (Fig. 10(f)). Centeno et al. [36] assigned the 2110 and 2143 cm^{-1} bands to the carbonyls formed with the participation of ultrafine gold clusters and Au^+ ions from the surface of metal particle, respectively. Pozdnyakova et al. [53] and Bogdanchikova et al. [54] assigned the 2177 cm^{-1} band to the carbonyl formed with the participation of isolated Au^+ and/or Ce^{+4} ions. Carbon monoxide does not interact with the ceria sites of the Ce_xO_y/Al_2O_3 catalyst (Fig. 10(a) and weakly interacts with the Au^0 sites (Fig. 8(c) at low CO pressure. Hence, we can assign the 2146 and 2176 cm^{-1} bands to the $Au^{\delta+}$–CO ($0 < \delta < 1$) complex in the $Ce_xO_y/Au/Al_2O_3$ catalyst.

The XPS spectra of Cu 2p and Ce 3d region for copper and cerium-contained catalysts after the reaction were almost similar to the XPS spectra presented in Figs. 7 and 9. The value of Au 4f $_{7/2}$ binding energy for the bimetallic catalysts after the reaction decreased, indicating that the relative $Au^{\delta+}$ content in the catalysts after the reaction was lower than that in the initial catalysts, which is illustrated in Fig. 12. The observed trend can be explained by the reduction of cationic gold by CO at high temperatures, which is described in numerous publications [31–37].

3.4. CO oxidation

The monometallic Au and M_xO_y catalysts showed activity in CO oxidation only in the 250–450 °C range. Passing of CO over bimetallic Au–M_xO_y catalysts resulted in

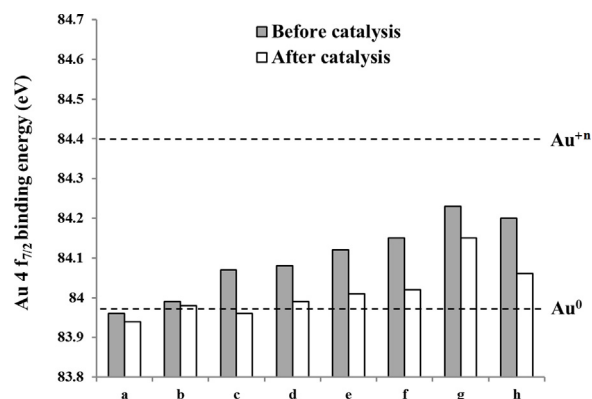**Fig. 12.** Oxidation states of gold in catalysts before and after the reaction at 450 °C. (a) Au/Al_2O_3 (IMP); (b) Au/Al_2O_3 (DP); (c) ($Au + Cu_xO_y$)/Al_2O_3; (d) ($Au + Ce_xO_y$)/Al_2O_3; (e) $Au/Cu_xO_y/Al_2O_3$; (f) $Au/Ce_xO_y/Al_2O_3$; (g) $Cu_xO_y/Au/Al_2O_3$; (h) $Ce_xO_y/Au/Al_2O_3$.

accumulation of CO_2 even at 50 °C (Fig. 13). These results illustrate the strong synergistic effect observed in the presence of bimetallic catalysts. The CO conversion measured at a specified temperature in the 50–450 °C range changes in the series: $Cu_xO_y/Au/Al_2O_3$ > $Ce_xO_y/Au/Al_2O_3$ > $Au/Cu_xO_y/Al_2O_3$ > $Au/Ce_xO_y/Al_2O_3$ > $Au + Ce_xO_y/Al_2O_3$ > $Au + Cu_xO_y/Al_2O_3$, which indicates that the catalysts produced by sequential deposition of metals are more active than the catalysts produced by simultaneous metal deposition.

There are some explanations proposed for the improvement in oxidation over bimetallic catalysts [19–22,31–37]. According to one explanation, the interaction between gold and another transition metal results in the formation of a new substance (alloy, solid solution, intermetallic compound, etc.). It is believed that these substances possess the enhanced reactivity [31–35]. At the first approximation, we can exclude this explanation from consideration, because the results of XRD analysis do not confirm the formation of new phases in our catalysts. According to the other explanation, the gold particle size plays an important role in an enhancing of bimetallic catalysts activity [31–37]. There are a lot of experiments illustrating the high reactivity of SML gold particles in CO oxidation [19]. The high catalytic activity observed for small gold clusters is explained in terms of quantum and structural size effects. The quantum size effect is usually manifested in 0.1–3 nm
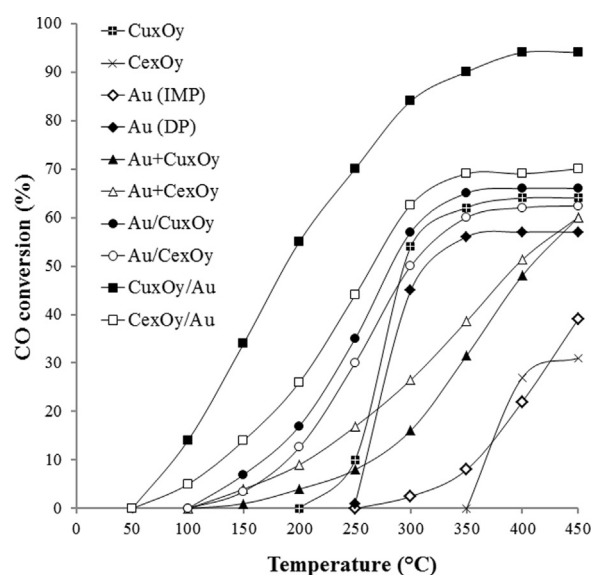

Fig. 13. CO oxidation over mono- and bimetallic catalysts supported on alumina.
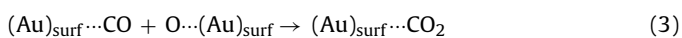
range and states that a decrease in the metal particle size results in changes of the electronic structure of atoms on the particle surface, which stimulates better CO and O_2 activation [60,61]. The structural size effect is observed in 0.5–60 nm range and states that a decrease in the particle size results in increase in the percentage of corner and edge atoms in the surface, which favors CO and O_2 activation [20,26,62,63]. Finally, the NSPH particles with rough shape are also proposed for the explanation of synergistic activity [20].

There is a good correlation between the high concentration of SML and NSPH particles observed for the bimetallic catalysts and the activity of these catalysts (Fig. 13, Table 2). This correlation indicates that the size effects and rough shape of the particles take an important part in the formation of the most active sites of the bimetallic catalysts.
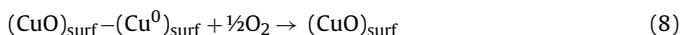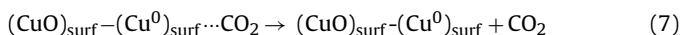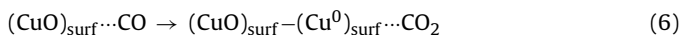
Note that the CO oxidation in the presence of the $(Au + Cu_xO_y)/Al_2O_3$ catalyst with 20 nm particles starts at about $50\,°C$. The CO oxidation in the presence of the Au/Al_2O_3 catalyst with 15 nm particles and Cu_xO_y/Al_2O_3 with 3 nm particles starts at about $250\,°C$. Next, in the 50–250 °C range, all bimetallic catalysts have exhibited high synergistic gain, which is calculated as the difference between CO conversion over bimetallic catalyst and the sum of CO conversions over its monometallic precursor measured at a specified temperature [56]. At high temperatures, the synergistic gain decreased (Fig. 13). These results indicate that the size and shape of particles are not the only factors responsible for the synergistic activity, and that electronic properties of supported metals as well as CO oxidation mechanism should also be taken into consideration.

It was reported [19–22,64,65] that the dominant mechanisms of CO oxidation on the gold and metal oxide surfaces are the Langmuir–Hinshelwood (L–H) and Mars van Krevelen (MvK) type mechanisms, respectively. The main steps of the L–H mechanism on the surface of Au nanoparticles $(Au)_{surf}$ are presented in Eqs. (1)–(4). The main steps of the MvK mechanism on the surface of CuO nanoparticles $(CuO)_{surf}$ are presented in Eqs. (5)–(8).
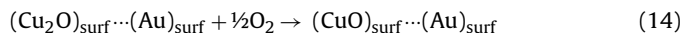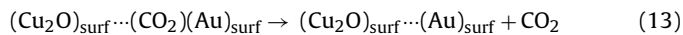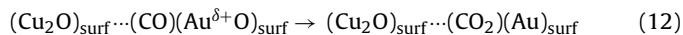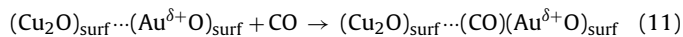
Langmuir–Hinshelwood (L–H) mechanism:

$$\tfrac{1}{2}O_2 + (Au)_{surf} \rightarrow O\cdots(Au)_{surf} \tag{1}$$

$$CO + (Au)_{surf} \rightarrow (Au)_{surf}\cdots CO \tag{2}$$

$$(Au)_{surf}\cdots CO + O\cdots(Au)_{surf} \rightarrow (Au)_{surf}\cdots CO_2 \tag{3}$$

$$(Au)_{surf}\cdots CO_2 \rightarrow (Au)_{surf} + CO_2 \tag{4}$$

Mars van Krevelen (MvK) mechanism:

$$(CuO)_{surf} + CO \rightarrow (CuO)_{surf}\cdots CO \tag{5}$$

$$(CuO)_{surf}\cdots CO \rightarrow (CuO)_{surf}-(Cu^0)_{surf}\cdots CO_2 \tag{6}$$

$$(CuO)_{surf}-(Cu^0)_{surf}\cdots CO_2 \rightarrow (CuO)_{surf}-(Cu^0)_{surf} + CO_2 \tag{7}$$
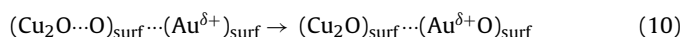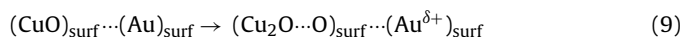
$$(CuO)_{surf}-(Cu^0)_{surf} + \tfrac{1}{2}O_2 \rightarrow (CuO)_{surf} \tag{8}$$

Some authors reported that the CO oxidation over bimetallic catalysts may differ from L–H and MvK mechanisms and occurs in Au–M sites with specific electronic organization [20,32–34,66]. It sounds reasonable because the electronic state of the metal strongly influences the adsorption of reactants and the rate of catalytic redox cycles. According to the specific electronic features of our bimetallic catalysts, here we propose the most probable mechanism for the synergistic CO oxidation. The main steps of this mechanism exemplified by the interacting gold and copper oxide clusters are presented below and include CO oxidation on cationic gold (Cycle A, Eqs. (9)–(14)) and partially reduced metal oxide (Cycle B, Eqs. (15)–(18)).
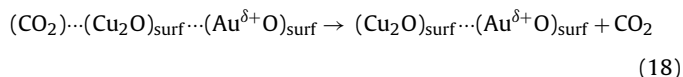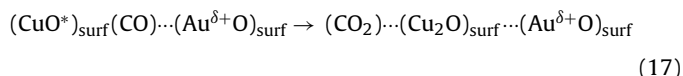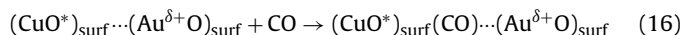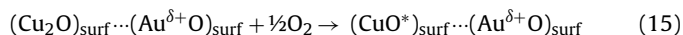
Synergistic mechanism, Cycle A – oxidation over $Au^{\delta+}$ sites:

$$(CuO)_{surf}\cdots(Au)_{surf} \rightarrow (Cu_2O\cdots O)_{surf}\cdots(Au^{\delta+})_{surf} \tag{9}$$

$$(Cu_2O\cdots O)_{surf}\cdots(Au^{\delta+})_{surf} \rightarrow (Cu_2O)_{surf}\cdots(Au^{\delta+}O)_{surf} \tag{10}$$

$$(Cu_2O)_{surf}\cdots(Au^{\delta+}O)_{surf} + CO \rightarrow (Cu_2O)_{surf}\cdots(CO)(Au^{\delta+}O)_{surf} \tag{11}$$

$$(Cu_2O)_{surf}\cdots(CO)(Au^{\delta+}O)_{surf} \rightarrow (Cu_2O)_{surf}\cdots(CO_2)(Au)_{surf} \tag{12}$$

$$(Cu_2O)_{surf}\cdots(CO_2)(Au)_{surf} \rightarrow (Cu_2O)_{surf}\cdots(Au)_{surf} + CO_2 \tag{13}$$

$$(Cu_2O)_{surf}\cdots(Au)_{surf} + \tfrac{1}{2}O_2 \rightarrow (CuO)_{surf}\cdots(Au)_{surf} \tag{14}$$

The first step of Cycle A should be the transfer of electron density from gold to the metal oxide (Eq. (9)), because simultaneous formation of cationic gold and the partial reduction of CuO (or CeO_4) was detected for the bimetallic catalysts (see Section 3.3). Next, the active O atom released during the partial reduction of metal oxide should spill over from M to Au (Eq. (10)) due to higher stability of oxygen atoms on the gold surface [66]. Then, CO molecule is adsorbed on the cationic gold of the Au–M interface (Eq. (11)) and reacts with the O atom to form CO_2 (Eq. (12)). The CO_2 produced desorbs from the catalyst (Eq. (13)). Finally, the oxygen vacancies in the partially reduced metal oxide react with oxygen from the gas phase (Eq. (14)) and the Cycle A, comprising the $Au^{\delta+}$ sites (Eqs. (9)–(14)), is completed. Cycle A accounts for the high activity of gold in the bimetallic catalysts compared to the activity of gold in monometallic samples. The first reason for the high activity of gold at the Au–M interface is the formation of $Au^{\delta+}$ species, which provides more pronounced CO activation than Au^0 species [36]. The second reason concerns the L–H rate-limiting step. The oxidation over bare gold clusters is limited by the dissociative adsorption of molecular oxygen (Eq. (1)), because gold is not very active in the O—O bond scission [19–21,67]. According to Cycle A, the interaction between Au and partially reduced metal oxide results in the direct supplies of active oxygen to the gold surface (Eq. (10)), which should be beneficial for further CO reaction on gold clusters.

Of course, Cycle A should be accompanied by Cycle B, which occurs on the partially reduced metal oxide species (Eqs. (15)–(18)).

Synergistic mechanism, Cycle B – oxidation over the partially reduced metal oxide:

$$(Cu_2O)_{surf}\cdots(Au^{\delta+}O)_{surf} + \tfrac{1}{2}O_2 \rightarrow (CuO^*)_{surf}\cdots(Au^{\delta+}O)_{surf} \tag{15}$$

$$(CuO^*)_{surf}\cdots(Au^{\delta+}O)_{surf} + CO \rightarrow (CuO^*)_{surf}(CO)\cdots(Au^{\delta+}O)_{surf} \tag{16}$$

$$(CuO^*)_{surf}(CO)\cdots(Au^{\delta+}O)_{surf} \rightarrow (CO_2)\cdots(Cu_2O)_{surf}\cdots(Au^{\delta+}O)_{surf} \tag{17}$$

$$(CO_2)\cdots(Cu_2O)_{surf}\cdots(Au^{\delta+}O)_{surf} \rightarrow (Cu_2O)_{surf}\cdots(Au^{\delta+}O)_{surf} + CO_2 \tag{18}$$

The partially reduced metal oxide species should be beneficial for the CO oxidation. This suggestion is supported by the experiments carried out by the group of Huang and Tsai and White et al. [68,69]. Huang and Tsai have compared Cu, Cu_2O, and CuO powder catalysts in CO oxidation [68]. Only Cu_2O was found to be active at $140\,°C$. White et al. have tested the activity of Cu_2O/SiO_2 catalyst and the catalytic behavior of Cu_2O and CuO powder catalysts in CO oxidation [69]. The activity of catalysts at $180\,°C$ changed in the series: $Cu_2O/SiO_2 > Cu_2O \gg CuO$. Nagase et al. [65] showed that the copper oxidation number cycled between +2 and 0 during CO oxidation by the MvK mechanism over stable CuO (Eqs. (5)–(8)). For Cu_2O, the initial oxidation number changed from (+1) to (+2) and implied the formation of metastable CuO* [65]. Then, the CO oxidation occurs via a redox cycle between metastable CuO* and Cu_2O [65]. According to the MvK mechanism [64], the rate-limiting

step in the oxidation over M_xO_y is the withdrawal of lattice oxygen (Eqs. (6) and (17)). The CuO* species were found to be very active, because of their excellent ability to transport the surface lattice oxygen [64,65,68]. Therefore, the relatively high concentration of Cu_2O species in the Au–Cu catalysts enhances its activity due to acceleration of the rate-limiting step (Eq. (17)). A recent theoretical study [69] confirmed the high propensity of CO to be oxidized on Cu_2O (1 0 0) plane by rapidly consuming surface oxygen, which is in agreement with the cause for synergistic activity proposed in the present study (Cycle B, Eqs. (15)–(18)).

The synergistic oxidation on $Au^{\delta+}$ cationic gold of our Au–Ce catalysts can be described by a catalytic cycle that is similar to Cycle A and reaps the benefits provided by better CO adsorption and acceleration of the L–H rate-limiting step. The CO oxidation on partially reduced ceria species can be described by a catalytic cycle that is similar to Cycle B and implies the oscillation between the Ce^{3+} and Ce^{4+} oxidation states. The studies done by Shapovalov et al. [70], Chen et al. [71] and Škoda et al. [58] report that the Ce—O bond is weakened upon deposition of Au on ceria. The weak Ce—O bond in the Au–Ce catalysts is, of course, favorable for the withdrawal of active oxygen from their surface, accelerates the MvK limiting step and, finally, enhances the CO oxidation on the Au–Ce catalysts compared with the Ce catalyst.

Now it is possible to discuss the whole set of data on the activity of our bimetallic catalysts (Fig. 13). The synergistic effect observed in the 50–250 °C range is caused by the CO oxidation over $Au^{\delta+}$ via Cycle A and over the partially reduced metal oxide species (i.e., Cu_2O and Ce_2O_3) via Cycle B. The high concentration of small and nonspherical gold particles also promotes CO oxidation. An increase in the reaction temperature from 250 to 280 °C accelerates the reduction of highly active cationic species in the bimetallic catalysts with carbon monoxide to less active species (i.e., Au^0 and M^0) but does not affect considerably the size and shape of the supported particles. As a result, the synergistic gain decreases in the 250–280 °C range. The increase in the reaction temperature above 280 °C induced a more pronounced decrease in the contents of $Au^{\delta+}$ and partially reduced metal oxide species. Moreover, the steric blockade of the Au–M interface by free Au or M_xO_y particles usually takes place at high temperatures [72]. The decrease in the contents of $Au^{\delta+}$ and partially reduced metal oxide species together with the steric blockade of the Au–M interface are the reasons for the absence of synergistic effect at 280–450 °C, although bimetallic catalysts still possess a good activity due to relatively high concentrations of small and nonsperical particles.

4. Conclusion

The general behavior of the surface chemistry and the catalytic action of Au–Cu and Au–Ce catalysts in the CO oxidation were established. The optimal structural and electronic organization is achieved in the $M_xO_y/Au/Al_2O_3$ catalysts and implies a high concentration of special sites: $Au^{\delta+}$ atoms at the Au–M interface; partially reduced metal oxide species at the Au–M interface; and atoms with a low coordination number on the surface of SML and NSPH particles. The $Au/M_xO_y/Al_2O_3$ catalysts possess a decreased concentration of the special sites. The smallest concentration of the special sites was found for the $(Au+M_xO_y)/Al_2O_3$ catalysts.

The CO oxidation in the presence of bimetallic catalysts starts at about 50 °C. The CO oxidation in the presence of monometallic Au/Al_2O_3 and M_xO_y/Al_2O_3 catalysts starts at about 250–350 °C, which clearly indicates the synergistic activity of the bimetallic catalysts. The cationic gold and partially reduced metal oxide species enhance the bimetallic catalyst activity due to the better adsorption of CO on $Au^{\delta+}$ sites, stabilization of O atoms on the gold surface and the acceleration of CO oxidation on the partially reduced metal

oxide species. The SML and NSPH particles are also beneficial for the activity of bimetallic catalysis due to their specific surface chemistry (i.e., high percentage of highly reactive corner and edge gold atoms). In the 50–250 °C range, all bimetallic catalysts have exhibited high synergistic gain, which is calculated as the difference between CO conversion over bimetallic catalyst and the sum of CO conversions over its monometallic precursor measured at a specified temperature. At high temperatures, the synergistic gain decreased. The reduction of $Au^{\delta+}$ species and the steric blockade of Au–M interface by free monometallic particles at higher temperatures are the general causes for decrease in the synergistic gain observed in the 280–450 °C range, although bimetallic catalysts still possess good activity due to relatively high concentration of small and distorted gold clusters.

Appendix A. Supplementary data

Supplementary data associated with this article can be found, in the online version, at http://dx.doi.org/10.1016/j.apcatb.2014.12.030.

References

[1] W.A. Bone, R.V. Wheeler, Phil. Trans. R. Soc. A 206 (1906) 1–67.
[2] R.S. Yolles, B.J. Wood, H. Wise, J. Catal. 21 (1971) 66–69.
[3] G.C. Bond, P.A. Sermon, Gold Bull. 6 (1973) 102–105.
[4] M. Haruta, T. Kobayashi, H. Sano, N. Yamada, Chem. Lett. 16 (1987) 405–408.
[5] P. Lakshmanan, P.P. Upare, N.-T. Le, Y.K. Hwang, D.W. Hwang, U.-H. Lee, H.R. Kim, J.-S. Chang, Appl. Catal. A 468 (2013) 260–268.
[6] S.A. Nikolaev, A.V. Chistyakov, M.V. Chudakova, V.V. Kriventsov, E.P. Yakimchuk, M.V. Tsodikov, J. Catal. 297 (2013) 296–305.
[7] X. Feng, X. Duan, G. Qian, X. Zhou, D. Chen, W. Yuan, Appl. Catal. B: Environ. 150–151 (2014) 396–401.
[8] X. Feng, X. Duan, G. Qian, X. Zhou, D. Chen, W. Yuan, J. Catal. 317 (2014) 99–104.
[9] P. Landon, P.J. Collier, A.J. Papworth, C.J. Kiely, G.J. Hutchings, Chem. Commun. (2002) 2058–2059, http://dx.doi.org/10.1039/B205248M.
[10] G.J. Hutchings, J.K. Edwards, Front. Nanosci. 3 (2012) 249–293.
[11] T. Tabakova, L. Ilieva, I. Ivanov, R. Zanella, J.W. Sobczak, W. Lisowski, Z. Kaszkur, D. Andreeva, Appl. Catal. B: Environ. 136–137 (2013) 70–80.
[12] M.G. Castaño, T.R. Reina, S. Ivanova, M.A. Centeno, J.A. Odriozola, J. Catal. 314 (2014) 1–9.
[13] S.A. Nikolaev, V.V. Smirnov, A. Yu Vasil'kov, V.L. Podshibikhin, Kinet. Catal. 51 (2010) 375–379.
[14] S.A. Nikolaev, N.A. Permyakov, V.V. Smirnov, A. Yu Vasil'kov, S.N. Lanin, Kinet. Catal. 51 (2010) 288–292.
[15] V.V. Smirnov, S.A. Nikolaev, G.P. Murav'eva, L.A. Tyurina, A. Yu Vasil'kov, Kinet. Catal. 48 (2007) 265–270.
[16] I.L. Simakova, S. Yu. Solkina, B.L. Moroz, O.A. Simakova, S.I. Reshetnikov, I.P. Prosvirin, V.I. Bukhtiyarov, V.N. Parmon, D. Yu Murzin, Appl. Catal. A 385 (2010) 136–143.
[17] S. Gómez-Quero, F. Cárdenas-Lizana, M.A. Keane, J. Catal. 303 (2013) 41–49.
[18] F. Cárdenas-Lizana, D. Lamey, N. Perret, S. Gómez-Quero, L. Kiwi-Minsker, M.A. Keane, Catal. Commun. 21 (2012) 46–51.
[19] T. Takei, T. Akita, I. Nakamura, T. Fujitani, M. Okumura, K. Okazaki, J. Huang, T. Ishida, M. Haruta, Adv. Catal. 55 (2012) 1–126.
[20] M. Chen, D.W. Goodman, Chem. Soc. Rev. 37 (2008) 1860–1870.
[21] G.C. Bond, Gold Bull. 42 (2009) 247–259.
[22] Y. Zhen Ma, Sheng Dai, Nano Res. 4 (2011) 3–32.
[23] Y. Zhang, R.W. Cattrall, I.D. McKelvie, S.D. Kolev, Gold Bull. 44 (2011) 145–153.
[24] I. Laoufi, M.-C. Saint-Lager, R. Lazzari, J. Jupille, O. Robach, S. Garaudée, G. Cabailh, P. Dolle, H. Cruguel, A. Bailly, J. Phys. Chem. C 115 (2011) 4673–4679.
[25] J. Guzman, B.C. Gates, J. Am. Chem. Soc. 126 (2004) 2672–2673.
[26] T.V.W. Janssens, B.S. Clausen, B. Hvolbæk, H. Falsig, C.H. Christensen, T. Bligaard, J.K. Nørskov, Top. Catal. 44 (2007) 15–26.
[27] L.M. Molina, B. Hammer, Phys. Rev. B 69 (2004) 155424–155446.
[28] H.Y. Kim, G. Henkelman, J. Phys. Chem. Lett. 4 (2013) 216–221.

[29] Y. Gao, N. Shao, Y. Pei, Z. Chen, X.C. Zeng, ACS Nano 5 (2011) 7818–7829.
[30] R. Coquet, K.L. Howard, D.J. Willock, Chem. Soc. Rev. 37 (2008) 2046–2076.
[31] A. Wang, X.Y. Liu, C.-Y. Mou, T. Zhang, J. Catal. 308 (2013) 258–271.
[32] H.-L. Jiang, Q. Xu, J. Mater. Chem. 21 (2011) 13705–13725.
[33] O.G. Ellert, M.V. Tsodikov, S.A. Nikolaev, V.M. Novotortsev, Russ. Chem. Rev. 83 (2014) 718–732.
[34] A.K. Singh, Q. Xu, ChemCatChem 5 (2013) 652–676.
[35] X. Liu, A. Wang, X. Wang, C.-Y. Mou, T. Zhang, Chem. Commun. (2008) 3187–3189, http://dx.doi.org/10.1039/B804362K.
[36] M.A. Centeno, K. Hadjiivanov, Tz. Venkov, Hr. Klimev, J.A. Odriozola, J. Mol. Catal. A: Chem. 252 (2006) 142–149.
[37] A.N. Pestryakov, V.V. Lunin, N. Bogdanchikova, O.N. Temkin, E. Smolentsev, Fuel 110 (2013) 48–53.
[38] F.-C. Duh, D.-S. Lee, Y.-W. Chen, Mod. Res. Catal. 2 (2013) 1–8.
[39] N. Weiher, E. Bus, L. Delannoy, C. Louis, D.E. Ramaker, J.T. Miller, J.A. van Bokhoven, J. Catal. 240 (2006) 100–107.
[40] T.R. Reina, S. Ivanova, M.A. Centeno, J.A. Odriozola, Front. Chem. 1 (2013) 1–9.
[41] J. Lian, J. Ma, X. Duan, T. Kim, H. Li, W. Zheng, Chem. Commun. 265 (2010) 0–2652.
[42] Z. He, H. Lin, P. He, Y. Yuan, J. Catal. 277 (2011) 54–63.
[43] M.C. Biesinger, L.W.M. Lau, A.R. Gerson, R. St.C. Smart, Appl. Surf. Sci. 257 (2010) 887–898.
[44] A.A. Davydov, in: N.T. Sheppard (Ed.), Molecular Spectroscopy of Oxide Catalyst Surfaces, John Wiley & Sons Ltd, Chichester, England, 2003, pp. 1–668.
[45] J.E. Bailie, G.J. Hutchings, H.A. Abdullah, J.A. Anderson, C.H. Rochester, Phys. Chem. Chem. Phys. 2 (2000) 283–290.
[46] Y.-N. Wang, X. Duan, J. Zheng, H. Lin, Y. Yuan, H. Ariga, S. Takakusagi, K. Asakura, Catal. Sci. Technol. 2 (2012) 1637–1639.
[47] F. Aubke, C. Wang, Coord. Chem. Rev. 137 (1994) 483–487.
[48] C. Korsvik, S. Patil, S. Seal, W.T. Self, Chem. Commun. 105 (2007) 6–1058.
[49] D.R. Mullins, S.H. Overbury, D.R. Huntley, Surf. Sci. 409 (1998) 307–319.
[50] Y. Yang, Y. Jin, H. He, Zh. Ye, CrystEngComm 12 (2010) 2663–2665.
[51] M. Romeo, K. Bak, J. El Fallah, F. Le Normand, L. Hilaire, Surf. Interface Anal. 20 (1993) 508–512.
[52] W.L.S. Faria, C.A.C. Perez, D.V. César, L.C. Dieguez, M. Schmal, Appl. Catal. B: Environ. 92 (2009) 217–224.
[53] O. Pozdnyakova, D. Teschner, A. Wootsch, J. Kröhnert, B. Steinhauer, H. Sauer, L. Toth, F.C. Jentoft, A. Knop-Gericke, Z. Paál, R. Schlögl, J. Catal. 237 (2006) 1–16.
[54] N. Bogdanchikova, A. Pestryakov, I. Tuzovskaya, T.A. Zepeda, M.H. Farias, H. Tiznado, O. Martynyuk, Fuel 110 (2013) 40–47.
[55] A.N. Pestryakov, V.V. Lunin, A.N. Kharlanov, D.I. Kochubey, N. Bogdanchikova, A. Yu Stakheev, J. Mol. Struct. 642 (2002) 129–136.
[56] S.A. Nikolaev, D.A. Pichugina, D.F. Mukhamedzyanova, Gold Bull. 45 (2012) 221–231.
[57] Y. Sugano, Y. Shiraishi, D. Tsukamoto, S. Ichikawa, S. Tanaka, T. Hirai, Angew. Chem. Int. Ed. 52 (2013) 5295–5299.
[58] M. Škoda, M. Cabala, I. Matolínová, K.C. Prince, T. Skála, F. Šutara, K. Veltruská, V. Matolín, J. Chem. Phys. 130 (2009) 034703–034707.
[59] H. Klimev, K. Fajerwerg, K. Chakarova, L. Delannoy, C. Louis, K. Hadjiivanov, J. Mater. Sci. 42 (2007) 3299–3306.
[60] D.C. Meier, D.W. Goodman, J. Am. Chem. Soc. 126 (2004) 1892–1899.
[61] M. Valden, X. Lai, D.W. Goodman, Science 281 (1998) 1647–1650.
[62] G. Mills, M.S. Gordon, H. Metiu, J. Chem. Phys. 118 (2003) 4198–4205.
[63] Y. Xu, M. Mavrikakis, J. Phys. Chem. B 107 (2003) 9298–9307.
[64] S. Royer, D. Duprez, ChemCatChem 3 (2011) 24–65.
[65] K. Nagase, Y. Zheng, Y. Kodama, J. Kakuta, J. Catal. 187 (1999) 123–130.
[66] R. Grisel, K.-J. Weststrate, A. Gluhoi, B.E. Nieuwenhuys, Gold Bull. 35 (2002) 39–45.
[67] H. Shi, C. Stampfl, Phys. Rev. B 76 (2007) 75,327(1)–075327(14).
[68] T.-J. Huang, D.-H. Tsai, Catal. Lett. 87 (2003) 173–178.
[69] B. White, M. Yin, A. Hall, D. Le, S. Stolbov, T. Rahman, N. Turro, S. O'Brien, Nano Lett. 6 (2006) 2095–2098.
[70] V. Shapovalov, H. Metiu, J. Catal. 245 (2007) 205–214.
[71] Y. Chen, P. Hu, M.H. Lee, H. Wang, Surf. Sci. 602 (2008) 1736–1741.
[72] S.A. Nikolaev, V.V. Smirnov, Catal. Today 147S (2009) S336–S341.